Check for updates

ADVANCED FUNCTIONAL MATERIALS
www.afm-journal.de

Superior Thermoelectric Performance of Textured $Ca_3Co_{4-x}O_{9+\delta}$ Ceramic Nanoribbons

Itzhak I. Maor, Katharina Kruppa, Adi Rozencweig, Amir Sterzer, Frank Steinbach, Vadim Beilin, Bernd Breidenstein, Gennady E. Shter, Meirav Mann-Lahav, Armin Feldhoff, and Gideon S. Grader**

Calcium cobaltite $Ca_3Co_{4-x}O_{9+\delta}$ (CCO) is a promising *p*-type thermoelectric (TE) material for high-temperature applications in air. The grains of the material exhibit strong anisotropic properties, making texturing and nanostructuring mostly favored to improve thermoelectric performance. On the one hand multitude of interfaces are needed within the bulk material to create reflecting surfaces that can lower the thermal conductivity. On the other hand, low residual porosity is needed to improve the contact between grains and raise the electrical conductivity. In this study, CCO fibers with 100% flat cross sections in a stacked, compact form are electrospun. Then the grains within the nanoribbons in the plane of the fibers are grown. Finally, the nanoribbons are electrospun into a textured ceramic that features simultaneously a high electrical conductivity of 177 S cm^{-1} and an immensely enhanced Seebeck coefficient of 200 µV K^{-1} at 1073 K are assembled. The power factor of 4.68 µW cm^{-1} K^{-2} at 1073 K in air surpasses all previous CCO TE performances of nanofiber ceramics by a factor of two. Given the relatively high power factor combined with low thermal conductivity, a relatively large figure-of-merit of 0.3 at 873 K in the air for the textured nanoribbon ceramic is obtained.

1. Introduction

The rising demand for global energy is hampered by low utilization efficiency, since more than half of it is lost as waste heat (e.g., in industry and transportation engines).[1,2] In light of the increasing use of electricity, conversion of this waste heat to electricity could be beneficial. Such a thermoelectric (TE) energy harvesting can be performed using solid state devices, that enable direct generation of electric power when exposed to a heat source. Those TE devices are composed of legs of *p*-and *n*-type semiconducting, TE materials, whose thermoelectric performance must be improved to achieve better energy conversion efficiency and/or higher power output, depending on application requirements and available heat source.[1–3]

In order to evaluate the performance of a TE material and to draw comparisons with other material classes, the power

I. I. Maor, A. Rozencweig, A. Sterzer, V. Beilin, G. E. Shter, M. Mann-Lahav, G. S. Grader
Wolfson Department of Chemical Engineering
Technion – Israel Institute of Technology
Haifa 3200003, Israel
E-mail: grader@technion.ac.il

K. Kruppa, F. Steinbach, A. Feldhoff
Institute of Physical Chemistry and Electrochemistry
Leibniz University Hannover
Callinstraße 3A, D-30167 Hannover, Germany
E-mail: armin.feldhoff@pci.uni-hannover.de

B. Breidenstein
IFW – Institute of Production Engineering and Machine Tools
Leibniz University Hannover
D-30823 Garbsen, Germany

G. S. Grader
The Nancy & Stephan Grand Technion Energy Program (GTEP)
Technion – Israel Institute of Technology
Haifa 3200003, Israel

The ORCID identification number(s) for the author(s) of this article can be found under https://doi.org/10.1002/adfm.202304464

© 2023 The Authors. Advanced Functional Materials published by Wiley-VCH GmbH. This is an open access article under the terms of the Creative Commons Attribution-NonCommercial-NoDerivs License, which permits use and distribution in any medium, provided the original work is properly cited, the use is non-commercial and no modifications or adaptations are made.

DOI: 10.1002/adfm.202304464

16163028, 0, Downloaded from https://onlinelibrary.wiley.com/doi/10.1002/adfm.202304464 by Cochrane Germany, Wiley Online Library on [22/11/2023]. See the Terms and Conditions (https://onlinelibrary.wiley.com/terms-and-conditions) on Wiley Online Library for rules of use; OA articles are governed by the applicable Creative Commons License

factor $PF = \sigma \cdot \alpha^2$ and the dimensionless figure-of-merit $f = zT$ are determined, which are correlated as follows:

$$f = \frac{\sigma \cdot \alpha^2}{\Lambda} = \frac{\sigma \cdot \alpha^2}{\lambda} \cdot T = zT \quad (1)$$

The figure-of-merit, which was coined as zT by Ioffe (1957),[4] is related to the energy conversion efficiency of a TE material and can be calculated from the isothermal electrical conductivity σ, the Seebeck coefficient α and the open-circuited entropy conductivity Λ, while the power factor is proportional to the power output of the material and depends only on σ and α. The entropy conductivity Λ is linked to the traditional heat conductivity λ via the absolute temperature T and offers the advantage to consider zT as a material parameter, which relies only implicitly on the temperature. For simplification, the general term thermal conductivity is used in the further course of this work, which comprises the entropy conductivity and the heat conductivity.[5]

Developing a high-performance TE material for high-temperature applications in air demands an increase of the power factor and a reduction of the thermal conductivity. Especially for high-temperature applications, which target high electrical power output, the power factor is an important criteria in addition to the power conversion efficiency determined by zT, perhaps even with a higher significance in the assessment of TE material performances.[3,6,7] While the upper limit of zT has not been determined yet, most state-of-the-art TE materials have a maximum $zT \approx 1$–2 in their respective temperature range of operation.[2,6,8]

Until a few years ago, the focus in the field of TE materials, both from commercial and research point of views, was mainly on alloyed semiconductors.[2,6] Chalcogenides, such as Bi_2Te_3 and PbTe,[9] skutterudites,[10] half-Heusler compounds,[11] Zintl-phases,[12] and other intermetallic compounds are among the most common used TE materials, as they present relatively high zT values under low and intermediate operation temperatures (≈300–900 K).[6,13–16] However, from the scope of applicability, TE materials should possess not only the highest zT values but also high durability, high chemical stability (e.g., resistance to oxidation and to operation at high temperatures), no toxicity, and economical/commercial feasibility (e.g., contents of relatively inexpensive abundant elements and low production cost). Properties that are not necessarily presented in alloyed semiconductors.[1,2] For these reasons, in recent years the interest in oxides as TE materials, that meet these attributes, increased notably.

Although oxides mostly do not possess as high zT as alloyed semiconductors, oxides are highly advantageous in many other aspects. The high chemical and thermal stability in air enable a large temperature gradient to be applied across the materials and therefore compensates for their lower zT value. Moreover, oxides permit chemical and structural versatility that allows great flexibility in material design and preparation, they are much more environmental-friendly, and in terms of raw material's cost they are less costly.[1–3,17] Processing of oxide-based materials for high-temperature applications should not primarily focus on zT as they are inferior to other material classes, but on high powere factor to ensure the highest possible electrical power output.

A promising group of TE oxides are layered cobalt-oxides, which were discovered to have excellent *p*-type TE properties at high temperatures in air. Among these oxides, sodium cobaltite, $Na_xCo_2O_4$, has outstanding thermoelectric properties in all relevant thermoelectric parameters, but unfortunately it degrades rapidly when operated at high temperature in air. Next best to $Na_xCo_2O_4$ is calcium cobaltite, $Ca_3Co_{4-x}O_{9+\delta}$ (CCO), which is thermally stable up to 1200 K in air.[1–3,17]

Since its discovery as TE material, many works have been done to characterize CCO. It is generally concluded that processing/synthesis method and so resulted microstructure highly influence its anisotropic TE abilities and stability.[18,19] In accordance with this observation, in some works electrospinning (ES) of (1D) structured CCO was hitched to bring forward additional improvement in this regard.[20–22] Recently, we took this research a step forward investigating the effect of CCO nanofibers microstructure on its thermoelectric properties, with an attempt to improve its TE performance. In this work, mixed nanofibers and nanoribbons mats of polycrystalline $Ca_3Co_{4-x}O_{9+\delta}$ were fabricated by sol–gel ES and calcination at intermediate temperatures (between 673 and 973 K) to obtain small primary particle sizes. These fibers were then pressed and compacted to calcined nanofibers bodies, which were measured thermoelectrically to determine their Seebeck coefficient and electrical conductivity. Subsequently, nanofibers bodies were also measured thermoelectrically during sintering to 1073 K (in situ sintering).[23]

Our work has revealed a pronounced dependence of nanofibers' microstructure on the synthesis parameters (ES precursor and process conditions). In comparison to other works, it is shown that under chosen ES parameters, resulted mat comprises both round nanofibers and flat nanoribbons,[23] rather than only round nanofibers.[20–22] It is also identified that calcination temperature has largely affected fibers phase microstructure and so TE performance. After calcination at 673 and 773 K fibers presented nanograined surface, but no distinct particles, and required phase is not reached. At 873 K fibers coarse surface with plate-like particles is presented and phase start to appear, when at 973 K fibers particles increased and a complete phase is reached.[23] TE wise, 973 K calcined fibers which were in situ sintered at 1073 K, exhibited an improved Seebeck coefficient of 176.5 S cm^{-1}. In addition, sample's power factor was 2.47 μW cm^{-1} K^{-2}, which is similar to an electrospun nanofiber-derived ceramic compacted by spark plasma sintering (SPS), presented by Yin et al.[21,23]

Ideally the TE structure could be built from flat building blocks that are laid parallel to each other, much like the construction of a brick wall. Most often, electrospinning gives rise to nanofibers with a round cross section, or a mixture of round, hollow, flat, and irregular cross section. Considering the results in the previous work, it is assumed that pure nanoribbons-based sample can show further improvement in TE properties of the compacted sample; primarily as compaction is expected to be better for flat fibers, but also by their possible contribution to texturing of the sample.

Nanoribbons formation by electrospinning was observed a few decades ago. Since then, in some works, a specific precursor composition and ES process parameters are shown to allow their formation.[24–26] In other works, ES parameters are varied in order to better explain the mechanism of nanoribbons formation (see **Table 1**). Mann-Lahav et al.[27] showed a

© 2023 The Authors. Advanced Functional Materials published by Wiley-VCH GmbH

Table 1. Precursors' compositions, electrospinning parameters, and resulted fibers morphology.

Reference	T [K]	RH [%]	V [kV]	TCD [cm]	Q [mL h^{-1}]	Needle inner diameter [mm]	Polymer	Polymer M_w [g mol^{-1}]	P/S (wt/wt.) $\times 10^2$	Solvents	Additional components (X/solvents) (wt/wt) $\times 10^2$	Fibers' cross-section shape
Koski et al. (2004)[31]	N/A	N/A	30	10.2	N/A	1.2	Polyvinyl alcohol (PVA)	9000–10 000	33.3	H_2O	No additives	Circle (with beads)
									53.8			Circle
								13 000–23 000	26.6			Circle
									33.3			Circle
									37.0			Circle
									44.9			Circle + rectangle
								31 000–50 000	33.3			Rectangle
								50 000–85 000	9.9			Circle
									12.4			Circle
									14.9			Rectangle
									20.5			Rectangle
								124 000–186 000	6.4			Circle
Zhao et al. (2005)[32]	N/A	N/A	10	20	N/A	1	Polyacrylamide (PAAm)	9 000 000	0.3	H_2O	sodium bis(2-ethylhexyl) sulfosuccinate (AOT)	Particles (not fibers)
									0.4, 0.5, 0.6		(0.03)	Circle (with beads)
									0.7, 0.91, 1.01, 1.52, 2.04			Circle + rectangle
									2.56			Rectangle
Neamnark et al. (2006)[34]	298	N/A	12	12	N/A	0.9	Hexanoyl chitosan	N/A	2.7	chloroform	No additives	beads
									4, 5.4, 6.7			Rectangle (with beads)
									9.4			Rectangle
Li et al. (2010)[33]	N/A	N/A	20	20	N/A	N/A	Polyvinyl-pyrrolidone (PVP)	1 300 000	4.4	H_2O : ethanol 1:1.3 (wt.)	$In(NO_3)_3 \cdot 4.5H_2O$ (4.4)	Circle
									4.6	H_2O : ethanol 1:2.6 (wt.)	$In(NO_3)_3 \cdot 4.5H_2O$ (4.6)	Circle + Rectangle
									9.2		$In(NO_3)_3 \cdot 4.5H_2O$ (9.2)	Rectangle

(*Continued*)

© 2023 The Authors. Advanced Functional Materials published by Wiley-VCH GmbH

16163028, 0, Downloaded from https://onlinelibrary.wiley.com/doi/10.1002/adfm.202304464 by Cochrane Germany, Wiley Online Library on [22/11/2023]. See the Terms and Conditions (https://onlinelibrary.wiley.com/terms-and-conditions) on Wiley Online Library for rules of use; OA articles are governed by the applicable Creative Commons License

Table 1. (Continued).

Reference	T [K]	RH [%]	V [kV]	TCD [cm]	Q [mL h^{-1}]	Needle inner diameter [mm]	Polymer	Polymer M_w [g mol^{-1}]	P/S (wt/wt.) $\times 10^2$	Solvents	Additional components (X/solvents) (wt/wt) $\times 10^2$	Fibers' cross-section shape
Wang et al. (2012)[29]	N/A	N/A	20	7	0.3	1.07	Nylon-6	35 000	6.4	formic acid (FA)	No additives	Circle (with beads)
									8.7, 13.6, 17.6, 22.0			Circle
									28.2			Rectangle
Jing et al. (2015)[35]	298	N/A	15	20	0.3	0.4	Polyvinyl-pyrrolidone	1 300 000	10.3	H_2O : ethanol 1:1.6 (wt.)	$Sr(NO_3)_2$, $Fe(NO_3)_3 \cdot 9H_2O$	Rectangle
							(PVP)		12.8		(9.9)	Rectangle
									15.4			Rectangle
He et al. (2015)[28]	N/A	N/A	8	18	N/A	N/A	Polyvinyl-pyrrolidone	1 300 000	17.5	ethanol : DMF	WCl_6	Circle
			10.5				(PVP)				(43.8)	Ellipse
			13							1:4.8 (wt.)		Ellipse
			15.5									Rectangle
			18									Rectangle
Stepanyan et al. (2016)[30]	296	30	43	16	1.5	0.7	Polyamide-6 (PA6)	16 000	11.1, 17.6, 25, 33.3	formic acid (FA)	No additives	Circle
								21 000	11.1, 17.6, 25, 33.3			Circle
								35 000	11.1			Circle
									17.6			Rectangle
Mann-Lahav et al. (2020)[27]	295–297	28–30	16–19	14.5	0.75	0.5	FAA-3 ionomer	N/A	56	DMF	No additives	Circle
									23.5	propanol		Rectangle
									40.8			Rectangle
Kruppa et al. (2023)[23]	293 303	45	25	12	1	0.34	Polyvinylpyrrolidone (PVP)	1,300,000	14.1	propionic acid: methanol 1:2.5 (wt.)	Co(CH3COO)2·4H2O (9.0) Ca(CH3COO)2·H2O (5.1)	Circle + Rectangle

© 2023 The Authors. Advanced Functional Materials published by Wiley-VCH GmbH

16163028, 0, Downloaded from https://onlinelibrary.wiley.com/doi/10.1002/adfm.202304464 by Cochrane Germany, Wiley Online Library on [22/11/2023]. See the Terms and Conditions (https://onlinelibrary.wiley.com/terms-and-conditions) on Wiley Online Library for rules of use; OA articles are governed by the applicable Creative Commons License

dependency of fibers structure (round or flat) in the ES precursors' solvents. Under conditions specified in Table 1, it was shown that cylindric fibers are formed when using higher boiling point solvent (dimethylacetamide—DMF, b.p. 426 K), while ribbons are formed using lower boiling point solvent (propanol, b.p. 370 K). Moreover, it was shown that flat fibers are obtained both in high and low polymer to solvent weight ratio (P/S), i.e., 0.408 and 0.235. He et al.[28] displayed a relation between applied voltage in the ES process and the formation of flat fibers. Cylindric fibers are obtained at relatively low voltage, and when gradually increased, fibers get elliptical and finally, above a threshold voltage, flat structure (Table 1). Both Wang et al.[29] and Stepanyan et al.[30] showed a dependency in polymer concentration or its molecular weight, i.e., precursor viscosity, on the formation of ribbons. According to their works, above a threshold viscosity cylindric fibers are no longer formed and replaced by ribbons (Table 1). In contrast, in early works, Koski et al.[31] and Zhao et al.[32] showed a gradual transition between cylindric fibers mat to a mixed round and flat fibers' mat and finally to a complete ribbons mat, by increasing the viscosity of the precursor (see details in Table 1). Li et al.[33] has presented similar trend, but they examined only 3 precursors that were different from each other in few parameters rather than only polymer concentration or molecular weight (see Table 1).

Based on the work done so far, the most accepted mechanism for the formation of flat ribbons by electrospinning, is composed of 3 main consecutive steps: 1) formation of dry polymer skin around an early stage (closer to the needle), wet fiber, 2) solvent evaporation from the round fiber's core through the tubular skin, and 3) collapse of resulted hollow tube to form a flat ribbon. Nevertheless, it is sometimes hard to find a common ground between processes in relation to this mechanism. For example, Mann-Lahav et al.[27] showed that ribbons are not formed using DMF as a solvent while they do form with propanol, claiming that propanol's lower boiling point enables the formation of the dry polymer skin in the way to ribbon formation. In contradiction, Fan et al.[25] and Koombhongse et al.[26] has managed to form electrospun ribbons using DMF as solvent for PVP and Polystyrene (280 000 g mo^{l-1}), respectively. It is therefore concluded that as ES is a multiparameter controlled process, there is probably more than one way (set of parameters) by which the above-mentioned mechanism is implemented to form flat nanoribbons.

Inspired by previous works, in the current work, we investigate the influence of polymer content in the ES precursor on the microstructure of raw CCO nanofibers, in an attempt to achieve pure nanoribbons' mat. Identifying a strong dependency of nanoribbons formation with polymer concentration in the ES precursor, we discuss the possible mechanism for this nanoribbon formation. Furthermore, we point to a key step in fibers calcination procedure to achieve their texturing. Microstructural examination is implemented for calcined nanoribbon bodies and sintered nanoribbon ceramics regarding texture, particle size, porosity, and density. Lastly, we link these microstructural features to the thermoelectric performance of the nanoribbon specimens by measuring Seebeck coefficient, electrical conductivity and thermal conductivity and determine the power factor *PF* and the figure-of-merit zT.

2. Results and Discussion

2.1. Nanofibers Characterization

To achieve pure electrospun nanoribbons' mat, the polymer concentration in the ES precursor was varied. Precursors with 0.06, 0.10, 0.14, 0.18, and 0.22 polymer to solvents weight ratio (P/S) were prepared (see Experimental Section). As expected, precursors showed an exponential increase in viscosity with increasing P/S (Figure S2, Supporting Information).[36] All precursors were electrospun under the same conditions (see Experimental Section). As shown in **Figure 1**, polymer concentration in the precursor, and so its viscosity, affects nanofiber structure drastically. Using precursor of P/S = 0.06, only thin cylindric fibers are formed (Figure 1a,b), but when P/S is increased, fibers in the mat gradually get thicker and more ribbon shaped fibers are formed (Figure 1). At a ratio of P/S = 0.22, 100% of the fibers become nanoribbons (Figure 1i,j). **Figure 2** shows a cross section of an uncalcined, raw nanoribbons mat, 0.2 mm in thickness, produced over a few hours of continuous stable electrospinning.

The fraction of round fibers and nanoribbons as a function of P/S ratio is shown in **Figure 3**a. The average perimeter of the round fibers and nanoribbons versus the P/S ratio is shown in Figure 3b. The trend of increased fraction of nanoribbons with increasing polymer concentration is in line with the findings of Koski et al.[31] and Zhao et al.[32] Koski et al.[31] suggested that flat fibers are formed as a result of the impact of relatively wet cylindrical fibers with the collector. This suggestion does not explain why a mixture of ribbons and cylindrical fibers can coexist in the same mat. In addition, it is expected that if the flattening mechanism is pure impact of wet fibers, the ribbons would be merged into each other. Such merging is not observed in Figure 2, where individual flat fibers are observed. Zhao et al.[32] ascribed the appearance of mixed fibers mat to the ultrahigh molecular weight of the polymer used (PAAm). They claimed that the polymer was not dispersed uniformly in the precursor solution, leading to nonuniform viscosity. As a result, the sections of high viscosity solution led to ribbon formation, while sections of low viscosity led to cylindrical fibers. This explanation however doesn't fit with the formation of pure ribbons mats using the highest polymer concentration in our work, and mixed round and ribbons mats at lower polymer concentrations, where PVP is completely and uniformly dissolved in the system of solvents.

We believe that this behavior is based on two well-known phenomena in electrospinning, 1) fibers diameter growth at higher precursor viscosities,[29,30,37] and 2) the existence of fibers diameter distribution in the collected mat.[38–40] We assume that during electrospinning, there is a threshold fiber diameter, D_{min}, above which ribbons can form by reported mechanism[26,41] where: 1) a polymer skin is formed over a wet fiber core, 2) solvents evaporate and the polymer is deposited on the inner skin surface forming a tube structure, and 3) tubes can collapses into a ribbons. When tubes collapse during flight, they are likely to twist and deform, and hence they will not stack parallel to each other on the collector. However, when examining our collected fibers (see Figures 1 and 2), at our highest P/S ratio, the fibers are not twisted but rather parallel to each other, which means that the fiber's final collapse into ribbons occurs on the collector.

© 2023 The Authors. Advanced Functional Materials published by Wiley-VCH GmbH

16163028, 0, Downloaded from https://onlinelibrary.wiley.com/doi/10.1002/adfm.202304464 by Cochrane Germany, Wiley Online Library on [22/11/2023]. See the Terms and Conditions (https://onlinelibrary.wiley.com/terms-and-conditions) on Wiley Online Library for rules of use; OA articles are governed by the applicable Creative Commons License

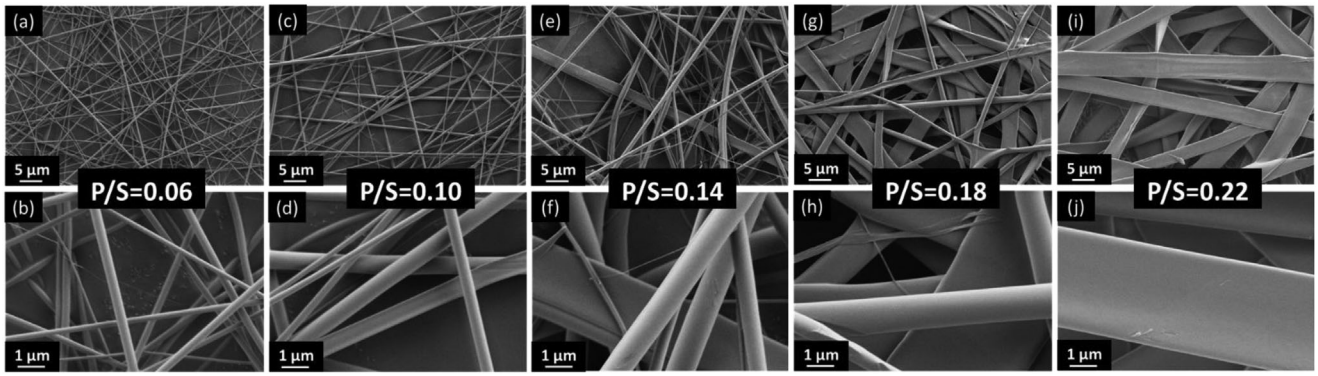

Figure 1. Top-view HRSEM images of raw, as electrospun, fibers made from precursors with varied polymer to solvents wt. ratio (P/S). a,b), c,d), e,f), g,h), and i,j) Low and high magnification images of fibers produced from precursors with P/S of 0.06, 0.10, 0.14, 0.18, and 0.22, respectively.

In earlier work we have done on branching effect during ES of PZT fibers,[42] we have shown that there is an order of magnitude difference in the time it takes the fibers to dry depending on their initial diameter. For thick and thin fibers with initial diameters of 1200 nm and 100 nm, the time to reach 10% of the initial concentration was 51 and ≈7.7 ms, respectively. In this work, we show that at a polymer to solvent ratio (P/S) of 0.22, the fiber's initial diameter (in the wet stage) is >3000 nm. The drying time, in this case, is expected to be considerably longer than 51 ms. We also show in **Figure 4** that the fiber dispersion cone during ES is much narrower at P/S = 0.22, again indicating that the fibers reach the collection surface faster than at lower P/S ratios. Hence, it is reasonable to hypothesize that during ES in this work, the fibers reach the collector before their full drying state. In effect the presence of methanol in the solvent facilitates fast evaporation from the surface, creating dried skin on the fibers. This ensures that the fibers do not merge into each other on the collector, which was not observed by SEM analysis. However, evaporation continues on the collector, which means that the fiber's final collapse into ribbons, occurs on the collector. This explains why the fibers stack parallel to each other as observed in Figure 2.

It is important to note that stretching and thinning of the fibers during their way to the collector is highly dependent on the viscosity, which is governed by the polymer concentration in the precursor solution or the P/S ratio. Fibers with different P/S ratios are expected to give rise to different ribbons. Due to greater stretching at lower viscosity, a lower P/S ratio (lower viscosity), will produce thinner and narrower ribbons. Therefore, ribbons from different P/S ratios in Figure 1, display a different width and thickness.

We believe that in the more viscous, high P/S ratio solutions, the polymer skin is thicker, keeping the initial large fiber diameter intact for longer time, facilitating the process of polymer skin formation and fiber collapse described earlier. In contrast, in less viscous solutions, the initial fiber can split more easily by the high voltage induced intrinsic electrostatic repulsion,[43] resulting in smaller diameter fibers, that are unable to form ribbons at all. This assumption is supported by the images taken during electrospinning and presented in Figure 4, showing the dramatic expansion of the fiber cloud as it moves toward the collector, when the precursor solution is less viscous (a lower P/S ratio). The thinner fibers in Figure 4a (P/S = 0.06) are more susceptible to repulsive forces, since their mass scales as the square of their radius. In addition, each fiber contains less charge (due to its smaller outer surface) and hence it moves more slowly in the electric field between the needle and the collector. Hence the repulsion between the fibers has sufficient time to expand the fiber cloud. On the other hand, the thick fibers in Figure 4e (P/S = 0.22) have more charge on each fiber and hence move faster toward the collector. In addition, the fibers are considerably heavier, and the repulsive force on them is less effective, and their cloud expands to a smaller extent. Modeling of the outer contour of the fiber cloud will be quite interesting, but beyond the scope of this paper.

To further explore ribbons formation in our system and based on the well-known phenomena of fibers diameter increase with lower process voltage,[37,43] we electrospun the precursors of

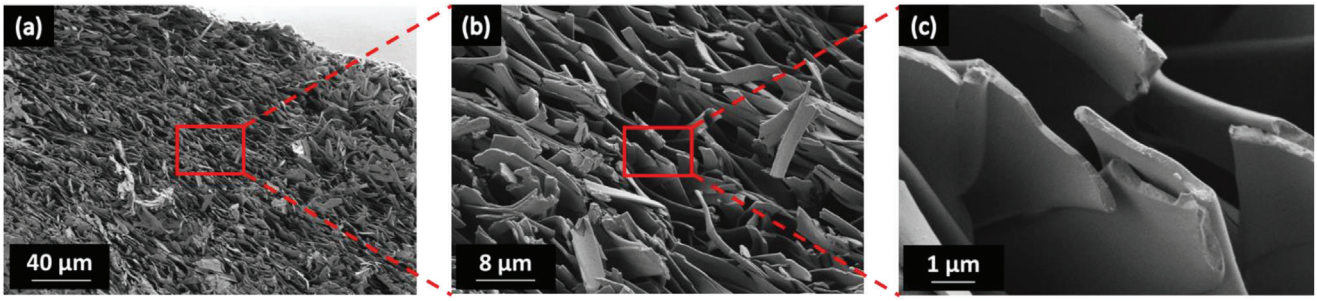

Figure 2. Cross sectional overview of raw, as electrospun, a) CCO ribbons mat made of 0.22 P/S precursor. b,c) Magnified images of (a).

© 2023 The Authors. Advanced Functional Materials published by Wiley-VCH GmbH

16163028, 0, Downloaded from https://onlinelibrary.wiley.com/doi/10.1002/adfm.202304464 by Cochrane Germany, Wiley Online Library on [22/11/2023]. See the Terms and Conditions (https://onlinelibrary.wiley.com/terms-and-conditions) on Wiley Online Library for rules of use; OA articles are governed by the applicable Creative Commons License

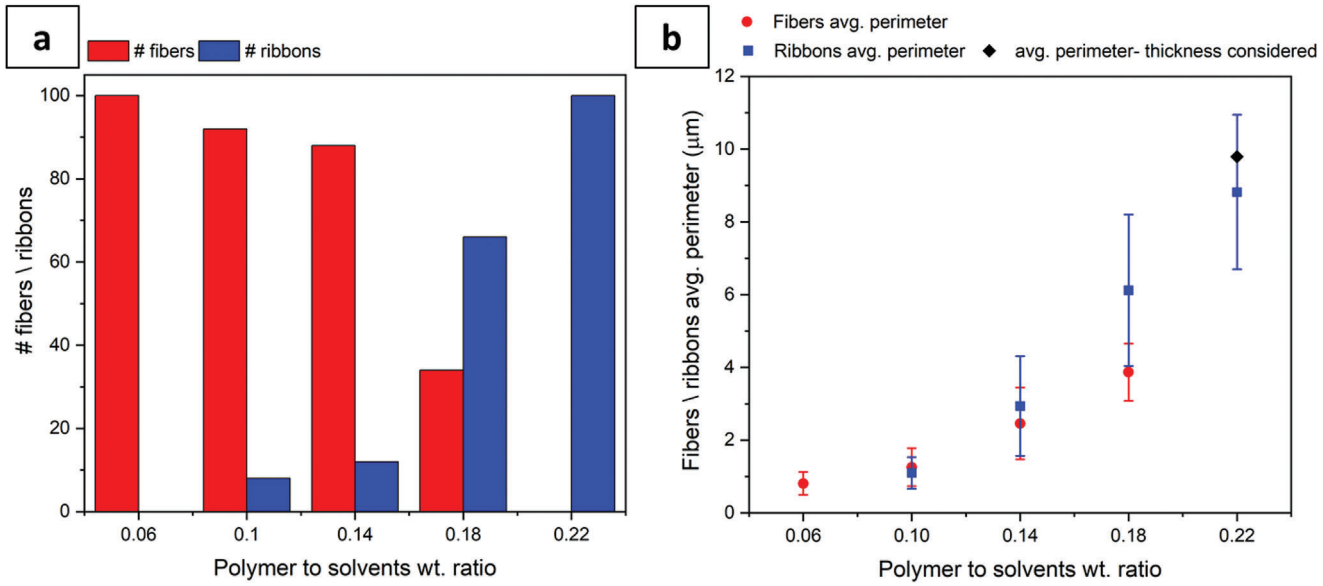

Figure 3. a) Fraction of nanofibers and nanoribbons in mats produced from precursors with P/S of 0.06, 0.10, 0.14, 0.18 and 0.22, and b) their average perimeter. Perimeter of cylindric fibers was calculated by $\pi \cdot$ fiber's diameter. The perimeter of ribbons was calculated by multiplying ribbon's width by 2, neglecting its thickness. For P/S = 0.22 sample, the thickness of ribbons was measured by images like in Figure 2. The average perimeter of this sample, considering the thickness of the ribbons, is marked as black diamond.

P/S = 0.10 and P/S = 0.18 under various voltages, to understand the influence of applied voltage on ribbons formation. Interestingly, between 15 and 24 kV, the applied voltage had relatively small influence on fibers diameter, ribbons width and their fraction in the formed mat, for the precursor of P/S = 0.10 (Figure S3b–e, Supporting Information). Below this voltages range (i.e., at 13 kV), only thick round nanofibers were obtained. Above this range, (i.e., at 27 kV), only thin round nanofibers were obtained (Figure S3a,f, Supporting Information). When the P/S ratio was increased to 0.18, round fibers became elliptical and finally flat with increasing voltage (Figure S4a–d, Supporting Information), consistent with Wang et al.[29] However, compered to Wang et al.[29] we never observed a complete ribbons mat at any voltage. On the contrary, above an applied voltage of 21 kV, the ribbons fraction decreased and thin cylindrical fibers appeared (Figure S4e,f, Supporting Information). A closer look on the fibrous structure of these two samples reveals torn section in the ribbons, probably due to internal Coulombic repulsion, and extra stretching resulting from the high voltage applied (Figure S5, Supporting Information), consistent with other works.[26,41]

To understand the thermal behavior of the green electrospun nanoribbons, TGA/DTA analysis of two samples were conducted under air flow up to 1173 K: fibers after initial drying at 353 K and after pre-heating at 523 K. The results are presented in Figure S6 (Supporting Information) along with detailed discussion of the heating stages, including solvents release, organics oxidative decomposition, Ca-carbonate decomposition with CO_2 release and CCO phase formation.

To obtain ceramic CCO nanoribbons, the raw ribbons mats were heated to burn out the organic components, form the required phase and sinter the fibers. The heating profile was selected based on the TGA/DTA results. We first performed the traditional calcination procedure, as done in previous work[23] (see procedure's stages in Figure S1a–d, Supporting Information), and obtained the ceramic CCO ribbons presented in **Figure 5**a–f. Unfortunately, during calcination the ribbons have

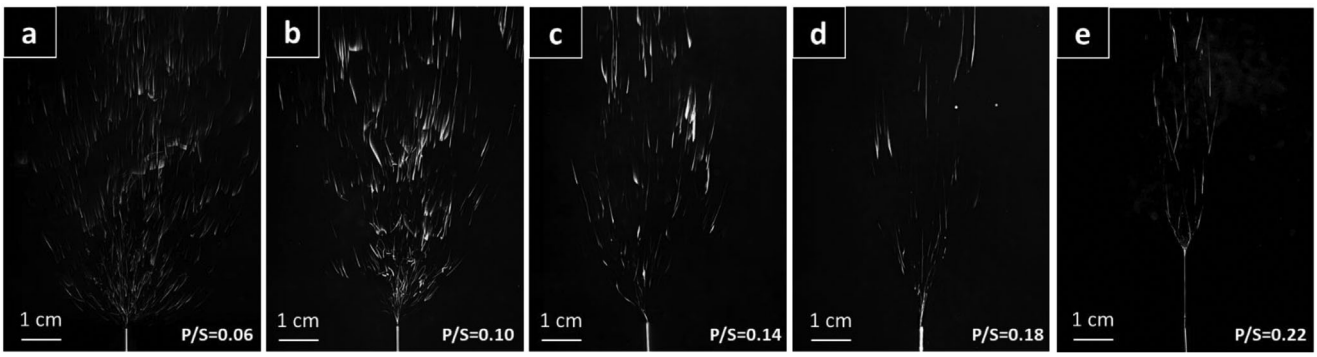

Figure 4. Images of electrospinning process preformed with precursor solution of P/S a) 0.06, b) 0.10, c) 0.14, d) 0.18, and e) 0.22.

© 2023 The Authors. Advanced Functional Materials published by Wiley-VCH GmbH

16163028, 0, Downloaded from https://onlinelibrary.wiley.com/doi/10.1002/adfm.202304464 by Cochrane Germany, Wiley Online Library on [22/11/2023]. See the Terms and Conditions (https://onlinelibrary.wiley.com/terms-and-conditions) on Wiley Online Library for rules of use; OA articles are governed by the applicable Creative Commons License

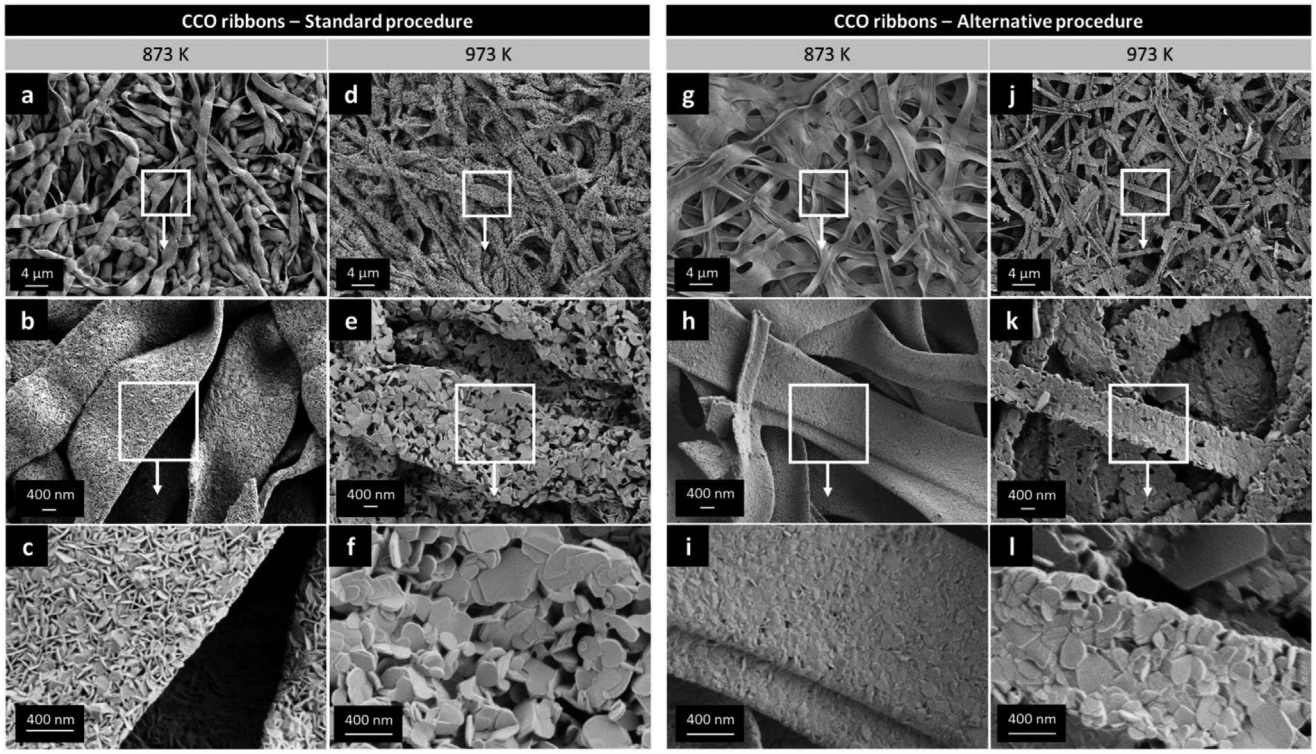

Figure 5. CCO ribbons calcined at 873 and 973 K, a–f) under standard and g–l) alternative thermal treatments.

dramatically shrunk and deformed, losing their flat orientation relative to each other. This phenomenon is attributed to polymer (PVP) relaxation during thermal treatment, mainly close to its glass transition temperature (T_g = 423–453 K).[44,45] In our case, deformation is even more drastic as the metal sources used in the precursor are highly hydrated (see Experimental Section), and when in contact with PVP, it's T_g is lowered significantly such that massive shrinkage starts at much lower temperature.[46,47] This phenomenon can be observed in Figure S1b (Supporting Information), where 2 × 2 cm^2 raw mat squares are slightly deformed during handling under ambient atmosphere, before calcination process.

For our purpose, those deformed ribbons are undesired as the loss of flat structure harms the ability to get compacted body and additionally looks like prefers the polycrystalline structure (Figure 5a–f, Supporting Information). To avoid ribbons deformation, an alternative thermal treatment was developed (see Figure S1a,e–h, Supporting Information). In this treatment we took advantage of the raw ribbons' adhesion to the ES substrate (100 µm aluminum foil), to fix the mat unshrunk over its glass transition temperature T_g (to a temperature of 523 K), where it starts to decompose. Then, mat pieces were moved to the box furnace and heated similarly to the standard procedure. This way, we managed to obtain flat undeformed CCO ribbons (Figure 5g–l). The shrinkage of mat pieces after temperature of 523 K and in the end of the process, at 973 K, in relation to the weight loss, for both alternative and standard processes was measured (Figure S7, Supporting Information). As expected, the major shrinkage part in the standard thermal treatment occurs between 353 K (mats' drying temperature) and 523 K (84%). In contrast, as determined by the mats' structure (Figure S1e, Supporting Information), in the alternative thermal treatment, a negligible shrinkage occurs in this temperatures range. At a final temperature of 973 K, shrinkage of 96.5% and 82% for standard and alternative thermal treatments, respectively, were observed. Interestingly, the final difference in shrinkage is relatively small (14.5%), but apparently it is enough to influence the microstructure notably.

Desirably, it seems that the different thermal treatment has also given rise to crystallites orientation (texturing). In comparison to standard thermal treatment, it looks that CCO platelets lay in ribbons plane. This observation was further tested by XRD and pole figure analyses.

2.2. Phase Identification, Microstructure, and Texture

Further characterization focusing on phase composition and microstructure were conducted on electrospun CCO nanoribbons, calcined and pressed nanoribbon bodies, and sintered nanoribbon ceramics. Electrospinning of flat nanoribbons targeted the alignment of anisotropic CCO primary particles prior to sintering to improve the electrical conductivity of TE ceramics in a preferred direction. Therefore, analyses were systematically directed to determine the texture of the primary particles in the nanoribbon specimens.

Figure 6 shows the XRD diffractograms of CCO nanoribbon mats calcined at 873 and 973 K, compared to their respective calcined nanoribbon bodies and ceramics. Presented are only nanoribbons specimens fabricated by the alternative thermal

© 2023 The Authors. Advanced Functional Materials published by Wiley-VCH GmbH

16163028, 0, Downloaded from https://onlinelibrary.wiley.com/doi/10.1002/adfm.202304464 by Cochrane Germany, Wiley Online Library on [22/11/2023]. See the Terms and Conditions (https://onlinelibrary.wiley.com/terms-and-conditions) on Wiley Online Library for rules of use; OA articles are governed by the applicable Creative Commons License

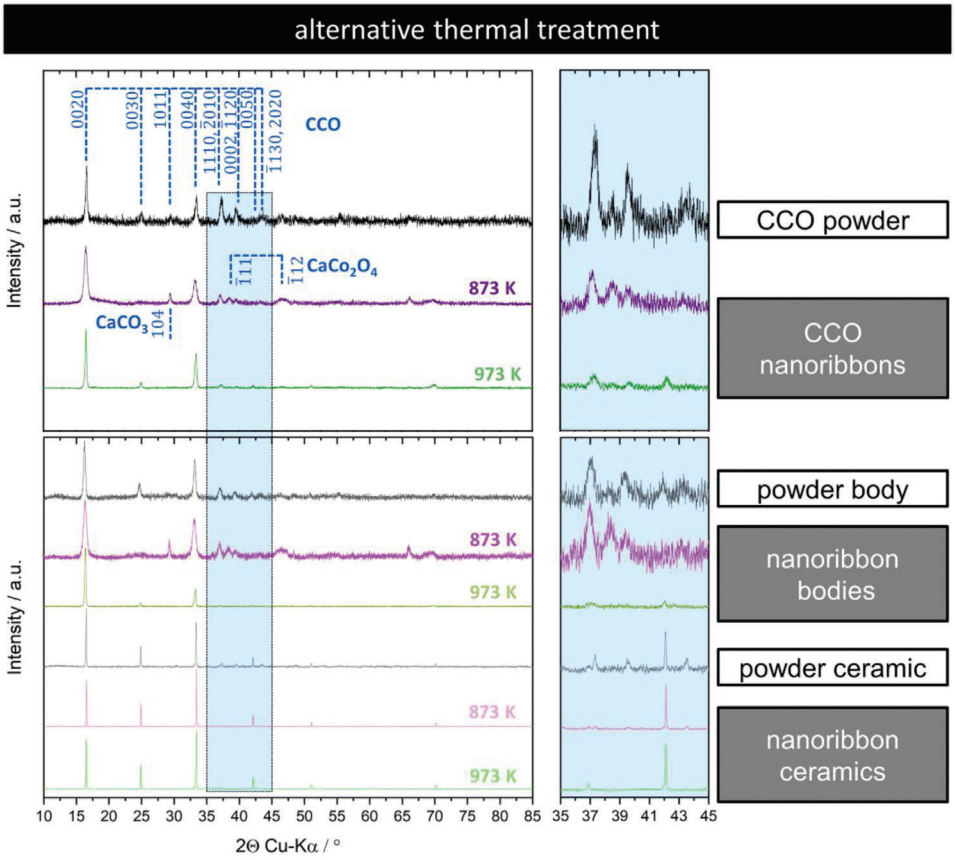

Figure 6. XRD diffractograms of $Ca_3Co_{4-x}O_{9+\delta}$ (CCO) powder, CCO nanoribbons calcined at 873 and 973 K with the alternative thermal treatment, calcined bodies and ceramics of the powder and nanoribbon specimens. XRD reflections were indexed using the indices of CCO corresponding to the four-dimensional superspace group *Cm* (0 1−*p* 0), explained;[23,48] monoclinic $CaCo_2O_4$ (PDF: [00-051-1760]); rhombohedral $CaCO_3$ (PDF: [00-024-0027]).

treatment (see Figure S1, Supporting Information). A commercial CCO powder with particle sizes up to 1 µm was also used as reference. Consistent with previous work,[23] the monoclinic CCO phase appears in the XRD diffractogram at a calcination temperature of 873 K, albeit with intermediates such as the monoclinic $CaCo_2O_4$ with additional peaks at 38° and 46° and the rhombohedral $CaCO_3$ with a peak at 29°. In contrast, the nanoribbon sample at 973 K occurs as single-phase CCO without impurities. The indexing of the XRD reflections of CCO was accomplished using the four-dimensional superspace group ***Cm*** (0 1−*p* 0) (equivalent to ***Bm***(0 0 *γ*) (No. 8.3)) in agreement with other published works.[23,48] In comparison to the powder, only the four-dimensional (00l0) reflections of the CCO phase are detectable in the XRD diffractograms of all nanoribbon specimens. This confirms texture being already present in the primary particles of electrospun and calcined nanoribbons, when the optimized thermal treatment is applied. The XRD diffractograms of the standard thermally treated nanoribbon specimens are included in the supporting information (Figure S8, Supporting Information), showing no texturing.

The (00l0) reflections in the XRD diffractograms of the here presented nanoribbon ceramics are even more pronounced, indicating stronger texture within the ceramic. Given the anisotropy of the layered CCO structure, the texturing is anticipated to improve the TE properties perpendicular to the pressing direction.[49,50,51]

In **Figure 7**, the microstructures of the nanoribbons and powder specimens are illustrated by SEM surface micrographs. The nanoribbons calcined at 973 K appear more porous than the samples calcined at 873 K, as can be seen in Figure 7a,b,d,e. More porosity is related to the accelerated growth of the primary particles in the nanoribbons at elevated temperatures, which are initially nano-grained and further increase to micrometer-sized particles during pressureless sintering.[23,52]

Strikingly, in Figure 7d,e, the microstructure of the nanoribbons is not initially lost, but integrated into the pressed nanoribbon bodies. In addition, the nanoribbons remain flat and stretched therein. This can be attributed to the alternative thermal treatment applied, in which the nanoribbon mats are fixed to the aluminum foil beyond the glass transition temperature T_g of the ES polymer up to a temperature of 523 K. As a result, the nanoribbons adhere stretched and unshrunk to the foil during pre-drying. On account of this effect and contrary to the CCO powder and respective pressed body and ceramic (see Figure 7f,i), a pronounced orientation of the plate-like grains preferentially perpendicular to the pressing direction and in the nanoribbons plane is observed on the surface of the nanoribbon ceramics (Figure 7g,h), which significantly reinforces our previous

© 2023 The Authors. Advanced Functional Materials published by Wiley-VCH GmbH

16163028, 0, Downloaded from https://onlinelibrary.wiley.com/doi/10.1002/adfm.202304464 by Cochrane Germany, Wiley Online Library on [22/11/2023]. See the Terms and Conditions (https://onlinelibrary.wiley.com/terms-and-conditions) on Wiley Online Library for rules of use; OA articles are governed by the applicable Creative Commons License

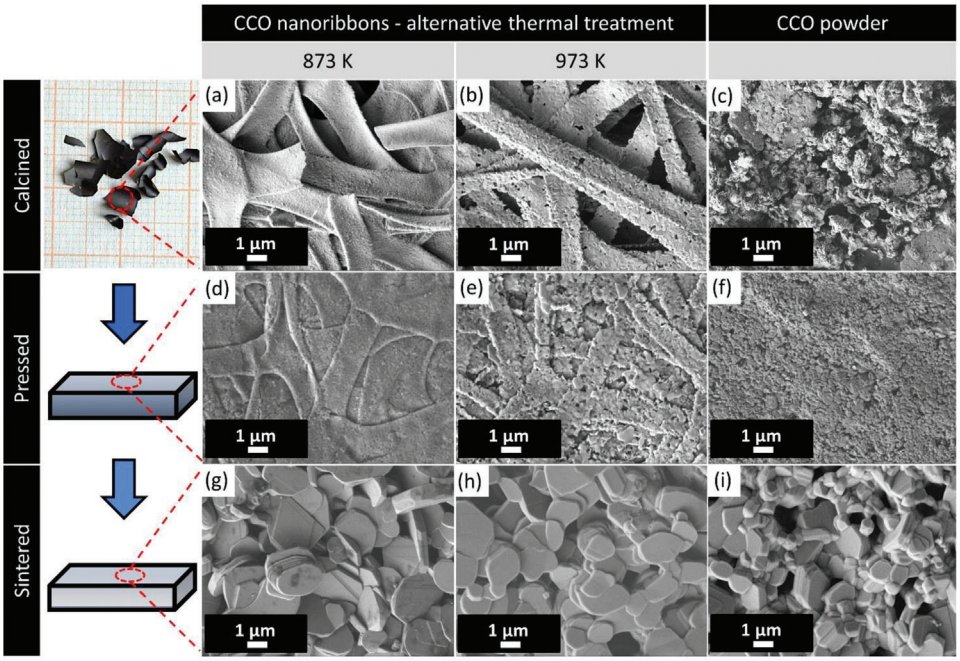

Figure 7. SEM surface micrographs of CCO nanoribbon mats, obtained with the optimized thermal treatment, calcined at a) 873 K and b) 973 K, c) CCO reference powder; Calcined bodies composed of cold-pressed CCO nanoribbons mats calcined at d) 873 K, e) 973 K, and f) CCO powder body; Nanoribbon ceramics of CCO nanoribbon mats pre-calcined at g) 873 K, h) 973 K, and i) CCO powder ceramic.

assumptions of texturing. This is not the case for the nanoribbon specimens calcined by standard thermal treatment. Thus, the SEM surface images in Figure S9 (Supporting Information) clearly show no stretched and flat nanoribbons but fractured by pressing. Correspondingly, the grains in the ceramic lack alignment, and hence no texturing was found, as also evidenced by the results of the XRD analysis in Figure S7 (Supporting Information), since all reflections are present. For additional comparison, fractured as well as polished SEM cross-sectional micrographs of the CCO powder and the nanoribbon ceramic, subjected to standard and alternative thermal treatment, were prepared (see Figures S10 and S11, Supporting Information). With the alternative treatment, a clear grain alignment pervading the entire nanoribbon ceramic is observed, leading to a strong texturing perpendicular to the pressing direction, whereas the powder and standard approach nanoribbon ceramic exhibit a random grain orientation, corroborating with the previous findings. Consequently, the thermal pretreatment of the green nanoribbon mats, involving nanoribbon's adhesion to the aluminum foil up to above the T_g of the ES polymer to counteract its polymer relaxation, has a crucial impact not only on the microstructure of the nanoribbons, but also on texturing in the final ceramics.[44]

Further analysis regarding the CCO nanoribbon ceramic pre-calcined at 973 K was performed by TEM measurements in **Figure 8**. The cross-sectional STEM micrographs and respective magnified images of the former CCO bar-shaped nanoribbon ceramic are given in Figure 8a–c, revealing a highly textured and porous structure. The TEM bright-field micrograph in Figure 8d exhibits the stacked assembly of the particles in the nanoribbon ceramic, and the difference in intensities of the corresponding TEM dark-field images in Figure 8e,f proves their high crystallinity. The STEM micrographs in Figure S12 (Supporting Information) were used to analyze the grain length and thickness in the ceramic. The sheet-like grains are quite large with 1–3 µm and the majority have a thickness of about 200–400 nm. However, as evident in Figure S13 (Supporting Information), very fine and thin grains with about 10 nm also exist, which would provide sufficient interfaces for phonon scattering.[53] Preserving small grain lengths on the nanometer scale is desirable to decrease the in-plane thermal conductivity (perpendicular to pressing direction) of the thermoelectric ceramic, but apparently not feasible with the applied pressureless sintering in this work. It requires other sintering techniques, such as SPS, to limit grain growth and maintain the nanostructure.[21,54]

Furthermore, the microstructures of both ceramics, powder and nanoribbons, feature a porous structure which can be traced back to the former porous nanoribbon structure itself and to the pressureless sintering. Therefore, the obtained relative densities of 55–68% (see **Table 2**) of the nanoribbon samples are lower than those received from SPS-sintered or pressure-assisted sintered CCO ceramics by Bresch et al.[55]

The CCO nanoribbon ceramic was also examined by HRTEM (Figure 8g,h), and SAED was conducted on an oriented grain along the zone axis [0100] (Figure 8i). The zone axis yielded a clear diffraction pattern with discrete diffraction spots of the site marked in Figure 8c, which enabled its definite indexing. No different orientation along the [0100] zone axis was observed for the studied grain. The HRTEM results in Figure 8g,h clearly indicate the stacking order along the *c*-axis, and the bright lines can be allocated to the CoO_2 layers of CCO.[56,57] The calculated *c*-axis dimension is 10.88 Å, which coincides with literature value of 10.83 Å for the CCO phase [PDF 00-058-0661, monoclinic]. From

© 2023 The Authors. Advanced Functional Materials published by Wiley-VCH GmbH

16163028, 0, Downloaded from https://onlinelibrary.wiley.com/doi/10.1002/adfm.202304464 by Cochrane Germany, Wiley Online Library on [22/11/2023]. See the Terms and Conditions (https://onlinelibrary.wiley.com/terms-and-conditions) on Wiley Online Library for rules of use; OA articles are governed by the applicable Creative Commons License

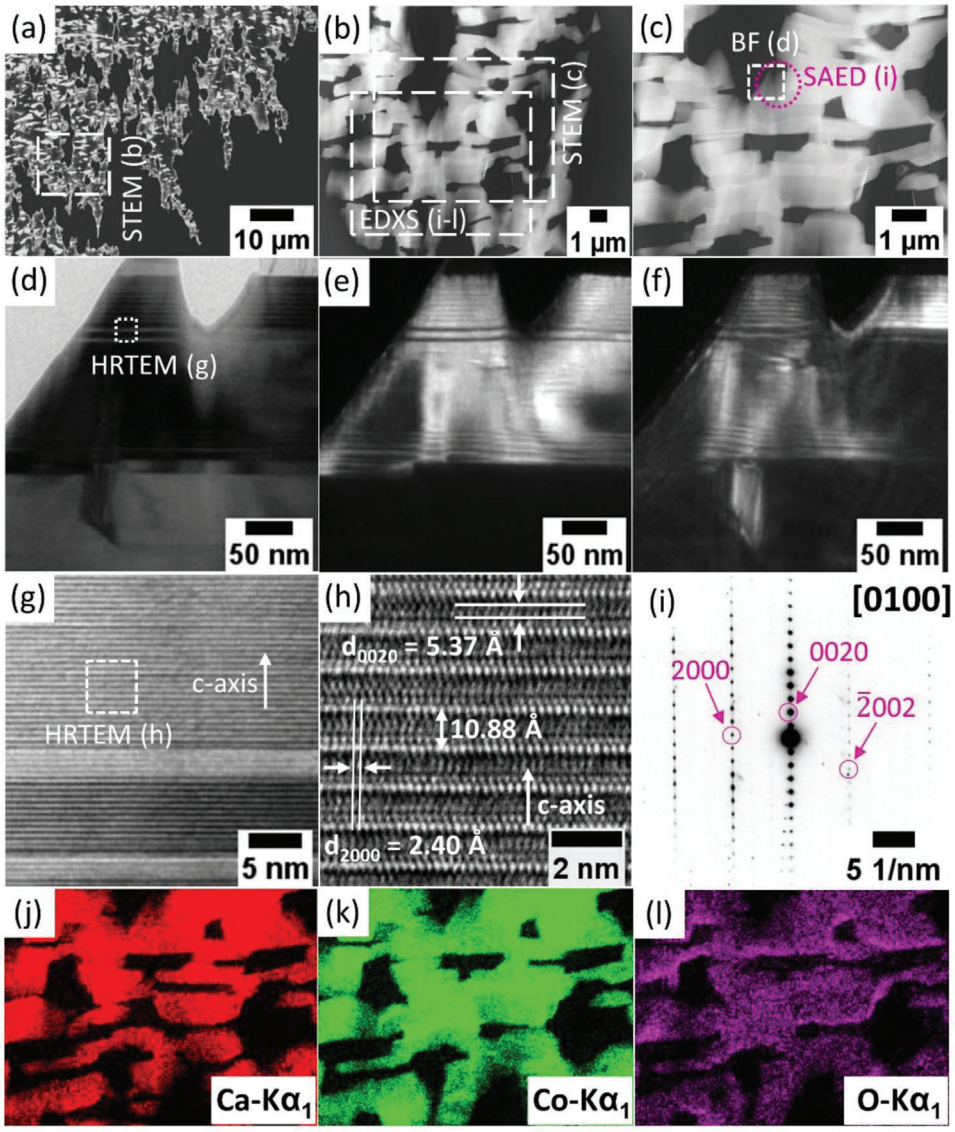

Figure 8. Cross-sectional TEM characterization of the nanoribbon ceramic calcined at 973 K. a) STEM annular dark-field micrograph (low magnification) and b,c) magnified STEM annular dark-field micrographs, showing textured particle arrangement and porous structure in the nanoribbon ceramic. d) TEM bright-field image, revealing stacked grains along the *c*-axis with e,f) corresponding TEM dark-field images, proving grains' high crystallinity. g,h) HRTEM micrographs, revealing (0020) and (2000) lattice planes, the stacking order along the crystallographic *c*-axis and its dimension. i) SAED pattern of oriented grain along the [0100] zone axis. j–l) EDXS mappings of aligned CCO grains from marked are in (b), showing homogeneous element distribution of Ca, Co, and O.

the HRTEM micrograph in Figure 8h, the lattice spacings of the CCO phase were identified and measure 5.37 Å between (0020) and 2.40 Å between (2000) lattice planes. The respective EDXS mappings of the tagged area in Figure 8b are shown in Figure 8j–l and verify a homogeneous elemental distribution of Ca, Co, and O within the CCO particles with no secondary phases.

In order to assess the degree of texture of the nanoribbon calcined bodies and ceramics in contrast to the powder specimens, quantitative texture analyses were performed, and the orientation distribution function (ODF) was determined. In **Figure 9**, the normalized XRD pole figures of the (0020) reflection calculated from the ODFs are presented. The pole figures obtained here are normalized to multiples of a random distribution (MRD) (see intensity scale bar in Figure 9), a unit that depends only on the orientation of the particles.[58,59,60,61] To quantify texturing, MRD values in the out-of-plane direction are computed via LaboTex using the evaluated ODF data. The maxima of the orientation densities indexed with MRD units for the samples are included in Table 2. The range of this unit is from no preferred alignment (1 MRD) to high MRD values, reminiscent of a high orientation density and strong texture.[55,61] The pole figures of the sintered nanoribbon ceramics and in particular the specimen pre-calcined at 973 K show a strong (00l0)-texturing with a maximum of 14.7 MRD, approximating a fiber texture. The pressing and subsequent sintering additionally increases the texture effect, as the only pressed nanoribbon bodies exhibit a lower

© 2023 The Authors. Advanced Functional Materials published by Wiley-VCH GmbH

16163028, 0, Downloaded from https://onlinelibrary.wiley.com/doi/10.1002/adfm.202304464 by Cochrane Germany, Wiley Online Library on [22/11/2023]. See the Terms and Conditions (https://onlinelibrary.wiley.com/terms-and-conditions) on Wiley Online Library for rules of use; OA articles are governed by the applicable Creative Commons License

Table 2. Multiples of a random distribution (MRD), relative density, porosity, Seebeck coefficient, electrical conductivity, and power factor of the calcined bodies (B) and ceramics (C) of nanoribbons calcined at 873 or 973 K and CCO powder. Thermoelectric values at 873 K and physical values at room temperature.

Specimens	MRD	Rel. density in %	Porosity in %	α in µV K^{-1}	σ in S cm^{-1}	PF in µW cm^{-1} K^{-2}
CCO powder B	6.6	62.9	37.1	207.3	51.7	2.22
CCO powder C	9.2	68.1	31.9	183.7	113.6	3.84
CCO NR 873 B	7.9	55.6	44.4	227.3	16.2	0.84
CCO NR 873 C	12.6	56.9	43.1	202.8	97.2	4.00
CCO NR 973 B	9.9	55.1	44.9	211.8	50.1	2.25
CCO NR 973 C	14.7	64.3	35.7	197.5	121.5	4.74

degree of texture (7.9–9.9 MRD). The CCO powder possesses a lower degree of particle orientation (9.2 MRD) and is inferior to the pressed nanoribbon sample pre-calcined at 973 K (9.9 MRD), showing that texturing is already promoted by the flat nanoribbon structure and the special thermal treatment prior to sintering. Pole figures of the (11$\bar{2}$1) reflections were also recorded for the specimens (see Figure S14, Supporting Information) but are weakly evolved due to the asymmetric samples dimension *xy* (see Figure 9) and respective insufficient sample size to provide a complete pole figure recording for this reflection.

2.3. Thermoelectric Characterization

The improved texture of ceramics from electrospun nanoribbon mats is expected to lead to enhanced thermoelectric properties compared to non-textured ceramics sintered from CCO powders. Therefore, the perpendicular to the pressing direction σ, α, λ, PF, and zT of the CCO nanoribbon and reference powder specimens were determined and are shown in **Figure 10**. We carefully deliberated on the appropriate orientation to assess the thermoelectric properties. We opted for the direction perpendicular to the

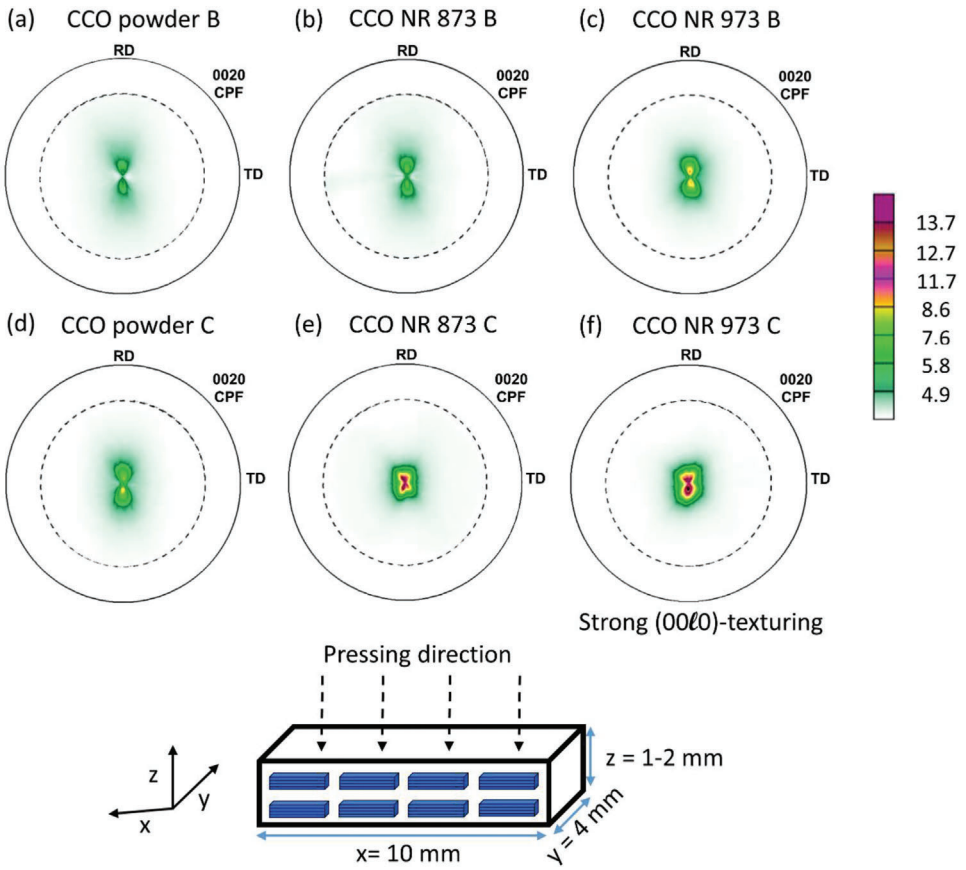

Figure 9. XRD pole figures (0020) (CPF = Corrected and preliminary normalized Pole Figure, TD = Transversal Direction, RD = Rolling Direction) with intensity scale of the MRD in a.u. obtained from calcined bodies B of a) CCO powder, nanoribbons calcined at b) 873 K and c) 973 K, ceramics C of d) CCO powder and nanoribbons mats pre-calcined at e) 873 K and f) 973 K.

© 2023 The Authors. Advanced Functional Materials published by Wiley-VCH GmbH

16163028, 0, Downloaded from https://onlinelibrary.wiley.com/doi/10.1002/adfm.202304464 by Cochrane Germany, Wiley Online Library on [22/11/2023]. See the Terms and Conditions (https://onlinelibrary.wiley.com/terms-and-conditions) on Wiley Online Library for rules of use; OA articles are governed by the applicable Creative Commons License

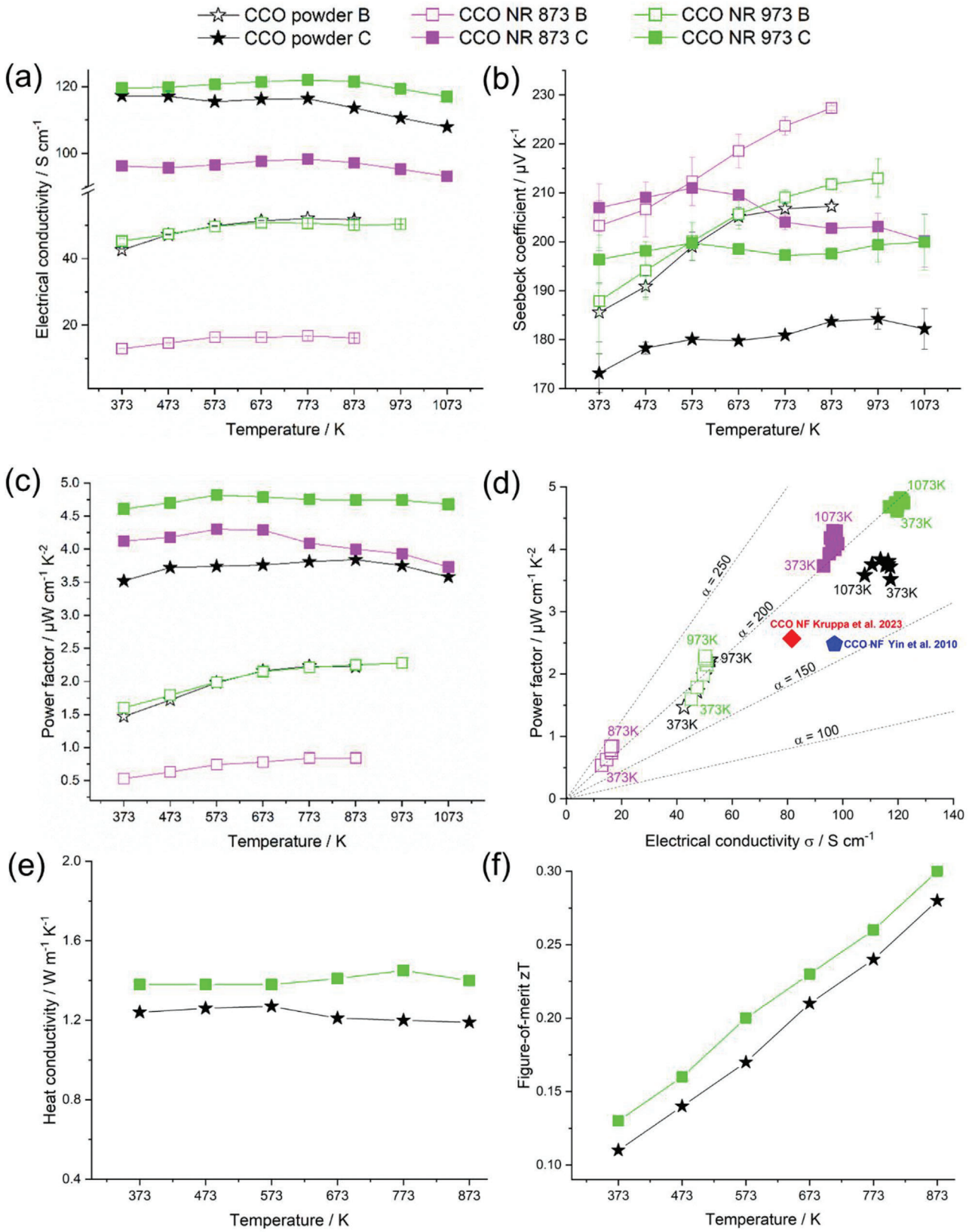

Figure 10. Thermoelectric properties of calcined CCO nanoribbon bodies B and ceramics C calcined at 873 and 973 K in comparison to the CCO powder. a) Electrical conductivity, b) Seebeck coefficient, c) Power factor PF, d) Type-I Ioffe plot showing the power factor as a function of the electrical conductivity, e) Thermal conductivity and f) Figure-of-merit *zT*.

© 2023 The Authors. Advanced Functional Materials published by Wiley-VCH GmbH

16163028, 0, Downloaded from https://onlinelibrary.wiley.com/doi/10.1002/adfm.202304464 by Cochrane Germany, Wiley Online Library on [22/11/2023]. See the Terms and Conditions (https://onlinelibrary.wiley.com/terms-and-conditions) on Wiley Online Library for rules of use; OA articles are governed by the applicable Creative Commons License

pressing direction due to the favorable orientation of both electrical conductivity and the Seebeck coefficient along the electronic-conducting CdI_2-type CoO_2 sheet. Although the thermal conductivity was also measured in this direction, it is worth noting that the direction parallel to the pressing direction encourages phonon scattering at the rock-salt-type Ca_2CoO_3 layers, resulting in a reduced thermal conductivity. In many cases, the figure-of-merit zT is determined by combining measurements from both directions in thermoelectric property evaluations, leading to an overestimation of zT. In contrast, our approach of measuring all properties in a single direction is more rational and yields more dependable outcomes.

Interestingly, the nanoribbon ceramic pre-calcined at 973 K shows a relatively high electrical conductivity of 177 S cm^{-1} and an enormously increased Seebeck coefficient of 200 μV K^{-1} at 1073 K. The electrical conductivity σ, displayed in Figure 10a, increases from the pre-textured nanoribbon bodies to the ceramics and exceeds the values of the non-textured powder specimens (see Figure S10, Supporting Information). The trend toward increased σ in the nanoribbon ceramics (Figure 9a) correlates with their stronger texture (higher MRD), due to grain orientation, and greater degree of density (see Figure S15, Supporting Information), both physical properties that were intensified by compaction and sintering.[55,62] Notably, while maintaining quite high electrical conductivity, the corresponding nanoribbon ceramics also generate very high Seebeck coefficients in the direction of the aligned grains, which is presumably also a result of the improved texture.[53,55,62] Bittner et al.[53] investigated the effect of texture on the thermoelectric properties of a porous CCO ceramic and found a positive effect on the Seebeck coefficient when grains are oriented. In particular, they examined the Seebeck coefficient parallel and perpendicular to the pressing direction and observed a significant difference depending on the direction, due to the texture obtained during compression. Direction-dependent measurements of the Seebeck coefficient were also explored by Kenfaui et al.[51] on a dense and highly textured CCO ceramic, who likewise revealed an anisotropic behavior with an increase in the direction of the texture.

Based on the values of the electrical conductivity and the Seebeck coefficient, the power factor was calculated to estimate the TE performance. The results in Figure 10c show that the textured ceramics, which were obtained from electrospun nanoribbons, achieve a 20% higher thermoelectric performance than the powder ceramic. Compared to CCO ceramics textured and sintered by other techniques, our electrospun nanoribbon sintered ceramics exhibit moderate electrical conductivity and simultaneously superior Seebeck coefficients, which places our reached power factor of 4.68 μW cm^{-1} K^{-2} at 1073 K in the upper mid-range (see Figure S16 and Table S1, Supporting Information for values from literature[19,21,23,50,54,55,59–61,63,64]). A higher reported Seebeck coefficient was achieved by Sotelo et al.[19] (235 μV K^{-1} at 1073 K), however, with a non-textured CCO ceramic and under diminution of the electrical conductivity (77 S cm^{-1}) which also reduced the power factor. The highest *PF* was achieved by Itahara et al.[50] for a textured CCO ceramic prepared by RTGG (reactive template grain growth) and tape casting. Nevertheless, it should be noted that hot pressing under oxygen atmosphere was chosen for sintering. It is also known from other work by Bittner et al.[17] that the best thermoelectric performance for a textured CCO ceramic is achieved if sintering is done under oxidizing conditions. The processing via O_2-sintering raises the oxygen content in the crystal structure of CCO, which increases the charge carrier concentration and thus the electrical conductivity. This behavior can be explained by the Brouwer diagram from Maier et al.[65] In the case of a *p*-type semiconductor such as CCO, the charge carrier concentration (holes) increases with the oxygen content resp. oxygen partial pressure in the phase, causing a higher electrical conductivity. Yu et al.[66] also highlights that annealing in O_2 favors electrical conductivity. They explain that the carrier concentration in CCO is reflected by the Co^{4+}/Co^{3+} ratio, with hole conduction (*p*-type) being regulated by the concentration of Co^{4+} in the CoO_2 layer of the CCO structure. Thus, one approach to enhance the electrical conductivity is to increase the carrier concentration via raising the average Co valence to Co^{4+}. This is done by reducing oxygen vacancies and increasing oxygen content in the CCO lattice by O_2-sintering. Despite this, investigations showed that the measured *PF* from O_2-sintered ceramics are not permanent in air, as some of the oxygen leaves the structure again, which lowers the oxygen content and reduces the electrical conductivity. The CCO phase sintered under O_2-atmosphere is thus not stable for applications at higher temperatures in air. Hence, the obtained *PF* should not be used as a benchmark for our nanoribbon ceramics, using pressureless sintering in air.[17,50]

Although the carrier concentration is intriguing and from significance, the texturing method presented in the manuscript and the subsequent enhancement of thermoelectric properties are valuable regardless of specific measurements such as the Hall effect. Additionally, it is important to note that CCO, being a well-known thermoelectric material, does not adhere to the Wiedemann–Franz relation (see Supporting Information). Consequently, techniques like nanostructuring and texturing are particularly emphasized for tailoring the thermoelectric properties. From the type-I Ioffe diagram in Figure 10d, which shows the *PF* as a function of electrical conductivity and Seebeck coefficient (dashed lines), it is evident that both the electrical conductivity and Seebeck coefficient are increased in the textured nanoribbon ceramic compared to the powder-derived ceramic. In addition, we see a significant improvement of the *PF* from the textured nanoribbon ceramic obtained from the calcination of nanoribbons, which exceeds that of other electrospun CCO materials like the mixed fiber (derived from the calcination of cylindrical nanofibers and flat nanofibers) ceramic from our previous work[23] (red diamond) and the dense SPS-sintered CCO nanofiber ceramic derived from only cylindrical nanofibers of Yin et al.[21] by a factor of two (see Figure 10d). This is based on the fact that the thermoelectric properties of the textured nanoribbon ceramic, both the electrical conductivity and the Seebeck coefficient are superior to those of the cylindrical nanofiber ceramic. Nonetheless, the increase in the electrical conductivity of the electrospun pure nanoribbon ceramics is particularly decisive for this result, not necessarily because of a higher density, but rather due to the strong texture, incorporated into the final TE ceramic as an outcome of the prior special thermal treatment of the flat nanoribbon mats and the resulting alignment of primary particles.

We also measured the thermal conductivity for the nanoribbon ceramic pre-calcined at 973 K and the powder ceramic, as displayed in Figure 10e. A special laminated steel holder was

© 2023 The Authors. Advanced Functional Materials published by Wiley-VCH GmbH

16163028, 0, Downloaded from https://onlinelibrary.wiley.com/doi/10.1002/adfm.202304464 by Cochrane Germany, Wiley Online Library on [22/11/2023]. See the Terms and Conditions (https://onlinelibrary.wiley.com/terms-and-conditions) on Wiley Online Library for rules of use; OA articles are governed by the applicable Creative Commons License

16163028, 0, Downloaded from https://onlinelibrary.wiley.com/doi/10.1002/adfm.202304464 by Cochrane Germany, Wiley Online Library on [22/11/2023]. See the Terms and Conditions (https://onlinelibrary.wiley.com/terms-and-conditions) on Wiley Online Library for rules of use; OA articles are governed by the applicable Creative Commons License

used to measure the thermal conductivity perpendicular to the pressing direction, along the texture direction. However, the maximum operation temperature of this special device is 873 K, which limited the temperature at which we could calculate the figure-of-merit, zT, of the material. We obtain slightly lower thermal conductivities with the CCO powder ceramic than with the nanoribbon ceramic. From Figure S17 (Supporting Information), which shows the entropy conductivity as a function of electrical conductivity and the T-dependent Lorenz numbers, it is noticeable that the CCO nanoribbon ceramics do not follow the empirical Wiedemann–Franz relation, as already mentioned, which normally describes a proportional relationship between electrical and thermal conductivity. Due to its layered structure and the individual functions of the layers, both the transport of charge carriers and phonons play an important role in the thermoelectric properties of CCO, and in particular the thermal conductivity is divided into a phonon and an electronic contribution. Enhancing the thermoelectric properties of CCO can be achieved through the process of nanostructuring and texturing the material. These techniques offer advantages by reducing the impact of phonons on thermal conductivity, mainly by introducing scattering centers at interfaces and grain boundaries. Remarkably, this improvement does not compromise the electrical conductivity, as demonstrated by the decrease of the entropy conductivity with increasing electrical conductivity of the CCO nanoribbons ceramic (Figure S17, Supporting Information) in the manuscript. The thermal conductivity in this context is not predominantly influenced by the movement of charge carriers but rather by the distinctive scattering behavior of phonons within the material. Consequently, the Wiedemann–Franz relation and corresponding slope of the Lorenz number depicted in Figure S17 (Supporting Information) (for a more detailed explanation refer to the Supporting Information) are not specifically applicable to the textured nanoribbon ceramic.[3,4,67] Nevertheless, we achieve a relatively low thermal conductivity for the nanoribbon ceramic of 1.4 W $m^{-1}K^{-1}$ at 873 K perpendicular to pressing direction, which is 2.7 times lower than estimated for textured CCO ceramic by Itahara et al.[50] and can be attributed to interfaces provided by the porous microstructure of our ceramic, which decreases thermal conductivity.[51,53] Part of the hypothesis is that the material–pore interfaces disrupt the charge carrier transport, which affects thermal conductivity.[21,53] It should be again noted that measurements of thermal conductivity are often performed parallel instead of perpendicular to the pressing direction. However, this underestimates the thermal conductivity, because the phonon transport is disturbed by the rock-salt type layer Ca_2CoO_3 in the crystal structure along the c-axis, which further decreases the phonon contribution and reduces the values by a factor of about 3, thus the zT value is overrated. This has been thoroughly examined in other publications performing anisotropy tests on textured CCO ceramics.[50,51,64] Owing to our comparatively high power factor and simultaneously low thermal conductivity, we gain a remarkably high and reliable zT of 0.3 at 873 K (Figure 10f) perpendicular to the pressing direction with the textured ceramic of the electrospun nanoribbon mats. It must be noted that the zT values in this work are provided only up to 873 K due to the above-mentioned equipment limitation caused by the special laminate specimen holder. However, consistent with the rise of zT with temperature seen in Figure S18 (Supporting Information), we expect a further increase of zT in our textured CCO samples at higher temperatures as well. In comparison to other zT values perpendicular to pressing direction of textured CCO ceramics published by Itahara et al.[50] with $zT = 0.12$ at 1060 (sintered in O_2) and Kenfaui et al.[51] with $zT = 0.16$ at 900 K (using hot-pressing in air), our results surpass theirs. Our ceramic nanoribbons sintered in air under pressure less conditions (see also Figure S18, Supporting Information), demonstrate an improvement by a factor of about 2 for the zT values. In particular, it should be noted that the zT of 0.16 at 773 K of pure cylindrical nanofiber ceramic by Yin et al.[21] is exceeded by 40 % with our pure flat nanoribbon ceramic.

3. Conclusions

In this work, we prepared thermoelectric (TE) $Ca_3Co_{4-x}O_{9+\delta}$ (CCO) fibers with 100% flat cross section by electrospinning (ES)under conditions that the fibers stacked parallel to each other on the collecting substrate, minimizing residual porosity. In addition, the compact stacking and pre-calcination on a rigid substrate did not allow the fibers to shrink. This in turn prevented twisting to the fibers and facilitated formation of well-textured nanostructured polycrystalline material, which can exhibit improved functional properties by making use of preferred crystallographic orientation.

The textured CCO nanoribbon ceramic features simultaneously a high electrical conductivity of 177 S cm^{-1} and an immensely enhanced Seebeck coefficient of 200 μV K^{-1} at 1073 K, resulting in a power factor of 4.68 μW cm^{-1} K^{-2} at 1073 K in air, which surpasses the performance of mixed round and flat nanofibers and SPS-sintered nanofiber TE ceramics by a factor of 2. These are therefore the best reported results for CCO nanofiber ceramics. In addition, compared to other textured CCO ceramics, we obtain a low thermal conductivity of 1.4 W m^{-1} K^{-1} at 873 K perpendicular to the pressing direction. Given our relatively high power factor combined with low thermal conductivity, we derive a strikingly large figure-of-merit, zT, of 0.3 at 873 K in air for the textured nanoribbon ceramic. The results reported here on improving the thermoelectric performance of CCO can be readily expanded to other ceramic systems, opening a new synthetic pathway toward high performance thermoelectric materials.

4. Experimental Section

Nanofibers Preparation: ES precursor solutions consisted of 1.00 g cobalt acetate tetrahydrate ($Co(CH_3COO)_2{\cdot}4H_2O$) (Acros Organics, Geel, Antwerp, Belgium) which was balanced by 0.53 g calcium acetate monohydrate ($Ca(CH_3COO)_2{\cdot}H_2O$) (Aldrich, St. Louis, MO, USA) to keep the required molar ratio (4:3) of $Ca_3Co_{4-x}O_{9+\delta}$. Both metal sources were mixed and stirred with propionic acid (Aldrich, St. Louis, MO, USA) (5.55 g) and absolute methanol (Bio-Lab, Jerusalem, Israel) (5.55 g) for 30 min until a homogenous purple solution was obtained. Then, different amount of polyvinylpyrrolidone (PVP) (M_w = 1 300 000 g mol^{-1}, Aldrich, St. Louis, MO, USA) was added to each solution, to achieve precursors with PVP/solvents wt. ratio of 0.06 (0.67 g), 0.10 (1.11 g), 0.14 (1.55 g), 0.18 (2.00 g), and 0.22 (2.44 g). All precursor solutions were stirred overnight and subsequently their viscosity was measured (DV-II, Brookfield, Middleboro, MA, USA). The as-prepared precursors solutions were electrospun (NS 24, Inovenso, Turkey) under applied voltage of 21 kV, with a tip to collector distance (TCD) of 15 cm, needle inner diameter of 0.34 mm and

© 2023 The Authors. Advanced Functional Materials published by Wiley-VCH GmbH

a precursor feed rate of 1 mL h^{-1}. The relative humidity inside the system container was 45% and the temperature was 296–300 K. The fibers mats were collected on an aluminum foil taped to the drum collector. After electrospinning, the fiber coated aluminum foils were dried overnight in a preheated (353 K) oven (PF60, CARBOLITE, Aston Lane/Hope, Sheffield, England).

Thermal treatments were conducted in a box furnace (LH 15/14 chamber furnace, Nabertherm, Lilienthal/Bremen, Lower Saxony, Germany) on the 0.22 PVP/solvents samples in two different procedures. First, a standard procedure, similar as performed by Kruppa et al.,[23] where after drying, mats are peeled off the aluminum foil, cut to ≈2 × 2 cm^2 squares, placed on a dense alumina plates and finally calcined at 873 and 973 K for 2 h (see Figure S1a–d, Supporting Information). Second, an alternative procedure, where mats are gradually dried in the drying furnace up to 523 K, then peeled off the aluminum foil, placed inside crucibles and calcined at 873 and 973 K for 2 h (see Figure S1a,e–h, Supporting Information).

Methods of Material Characterization: Photos of electrospinning, during operation, were taken by digital camera (A7 IV, Sony, Tokyo, Japan) equipped with macro lens (70–200 mm F2.8 GM II, Sony, Tokyo, Japan) and 2 back flash lights (HVL-F60RM2 (GN60), Sony, Tokyo, Japan). Photography specifications: f16 aperture, exposure time of 1/250 s, sensor sensitivity of 100 ISO and two flashes operated at full power. Raw and calcined nanofibers/ribbons were characterized using a high-resolution scanning electron microscope—HRSEM (ULTRA plus, Zeiss, Switzerland).

Thermal behavior of the electrospun CCO nanoribbons was investigated by simultaneous thermogravimetric and differential thermal analyses, TGA/DTA (SetSys 1750, Setaram, Caluire, France). Analysis was under air flow in the temperature range of 213–1173 K with heating rate of 5 K min^{-1}. Sample mass was 20–30 mg in alumina crucibles.

To obtain the compacts and ceramics for further examinations on microstructure, electrospun CCO nanoribbons mats were cold-pressed (200 MPa, 20 min) and sintered at 1073 K for 2 h in air. A commercial CCO powder ($Ca_3Co_4O_9$, CerPoTech, Norway) was used as reference. The microstructures of the nanoribbon compacts and sintered ceramics as well as the reference powder were investigated via field-emission scanning electron microscopy (FE-SEM, JEOL JSM-6700F) and field-emission transmission electron microscopy (FE-TEM, JEOL JEM-2100F-UHR). Elemental maps were obtained by an energy-dispersive X-ray spectrometer (Oxford Instruments INCA 200 TEM).

Fractured and polished cross sections were prepared for SEM by breaking off or cutting a slice from the pressed and sintered specimens. For the polished cross section, the slice was embedded in epoxy resin and a multistage polishing program with diamond lapping films (MultiPrep system, Allied High Tech Products, Inc.) was then performed with subsequent vibratory polishing using a 50-nm Al_2O_3 suspension. For TEM, cross sections of the nanoribbons mats were received by embedding a slice in epoxy resin, polishing from both sides to electron transparency with the diamond lapping films and 3 kV argon-ion polishing with a Precision Ion Polishing System (PIPS, Gatan Model 691). The phase identification of the nanoribbon mats and the reference powder as well as the pressed and sintered specimens was carried out by X-ray diffraction (XRD, Bruker D8 Advance) with Cu-$K\alpha$ radiation at 40 kV and 40 mA. To characterize the texture, the compacts and ceramics were subjected to measurement of the pole figures of the (0020) lattice planes according to the indexing of the four-dimensional space group Cm (0 1−p 0) (equivalent to Bm(0 0 γ) (No. 8.3))[48] (polar angle $\varphi = 0$–70°, increment $\Delta\varphi = 5°$; azimuthal angle $\theta = 0$–360°, increment $\Delta\theta = 5°$, integrating β-measurement 10 s · $5^{\circ -1}$) using XRD (3003 ETA 5-circle X-ray diffractometer, Seifert, Schnaittach-Hormersdorf, Germany) with Co-$K\alpha$ radiation (spot focus), a X-ray tube power of 30 kV and 40 mA, a 1 mm point collimator (helium filled) and a silicon drift detector (SDD) (AXAS-M, Ketek GmbH, Munich, Germany). The pole figure representation was conducted with the software LaboTex from the company LaboSoft, Krakow. The relative density and porosity of the samples were determined by the Archimedes method as described elsewhere.[23]

Thermoelectric Measurements Procedure: For investigating functional properties, pure CCO nanoribbons mats and the reference CCO powder were cold-pressed (500 MPa, 20 min) the nanoribbons mats and reference CCO powder into bar-shaped compacts with a length of 10 mm, a width of 4 mm and a thickness of 1–2 mm. The bar-shaped specimens with their longitudinal direction perpendicular to the pressing direction, were subjected to measurements of electrical conductivity, Seebeck coefficient and thermal conductivity, in both the only pressed and sintered state. The Seebeck coefficient was estimated under equilibrium conditions by using a ProboStat A (NorECS AS, Haslevollen, Norway) with a vertical furnace (Elite Thermal Systems Ltd., Market Harborough, UK). The electrical conductivity was determined with a four-point probe method under steady-state conditions using a measurement setup with platinum electrodes, KEITHLEY 2100 6/12 digital multimeters (Keithly Instruments, Solon, OH, USA) and a three-zone high-temperature tube furnace (Carbolite Gero EVZ 12/450B, Neuhausen, Germany). The respective values were recorded after heating to the maximum temperature of 873 and 973 K each for the pressed samples, corresponding to their previous calcination temperature, and 1073 K for the sintered samples and subsequent cooling steps of 100 K each down to room temperature with intermediate dwell times to retain stable conditions. The measurement setup consisted of an automated data collector with the software Lab View. Thermal conductivity was determined by measuring thermal diffusivity with a Light Flash Setup LFA 467 HT Hyper Flash (Netzsch, Selb, Germany) with an InSb detector and the density by Archimedes Setup. The required heat capacity C_p was taken from literature.[53] For the measurement perpendicular to pressing direction, a special laminate holder made of steel was used, which operates up to 873 K under argon atmosphere. Sample preparation required pressing of bar-shaped samples (10 × 4 × 2 mm), cutting samples with diamond wire saw to obtain cross sections (10 × 2 × 2 mm) and polishing the cross sections on both sides with the diamond lapping films (MultiPrep system, Allied High Tech Products, Inc.) for plane sample surface. The cross-sections were coated with graphite for the measurement.

Supporting Information

Supporting Information is available from the Wiley Online Library or from the author.

Acknowledgements

I.I.M. and K.K. contributed equally to this work. This work was financially supported by the Lower Saxony Ministry of Science and Culture in the frame of the Research Cooperation Lower Saxony-Israel, project number 2029896. This work was supported by the Nancy & Stephan Grand Technion Energy Program (GTEP). G.S.G. acknowledges the support of the Arturo Gruenbaum Chair in Materials Engineering. This research was supported by the Israeli Ministry of Energy as part of the scholarship's program for first to third degree students in the fields of energy. The authors would like to thank Kobi Goffer and Ilya Margulis for their help with capturing the photos of electrospinning process during its operation.

Open access funding enabled and organized by Projekt DEAL.

Conflict of Interest

The authors declare no conflict of interest.

Data Availability Statement

The data that support the findings of this study are available in the supplementary material of this article.

Keywords

electron microscopy, electrospinning, microstructure, thermoelectric properties, nanoribbons

© 2023 The Authors. Advanced Functional Materials published by Wiley-VCH GmbH

16163028, 0, Downloaded from https://onlinelibrary.wiley.com/doi/10.1002/adfm.202304464 by Cochrane Germany, Wiley Online Library on [22/11/2023]. See the Terms and Conditions (https://onlinelibrary.wiley.com/terms-and-conditions) on Wiley Online Library for rules of use; OA articles are governed by the applicable Creative Commons License

Received: April 23, 2023
Revised: July 8, 2023
Published online:

[1] R. Funahashi, T. Barbier, E. Combe, *J. Mater. Res.* **2015**, *30*, 2544.
[2] J. He, Y. Liu, R. Funahashi, *J. Mater. Res.* **2011**, *26*, 1762.
[3] M. Wolf, R. Hinterding, A. Feldhoff, *Entropy* **2019**, *21*, 1058.
[4] A. F. Ioffe, *Semiconductor Thermoelements and Thermoelectric Cooling*, Infosearch Ltd. , London **1957**.
[5] A. Feldhoff, *Entropy* **2020**, *22*, 803.
[6] A. J. Minnich, M. S. Dresselhaus, Z. F. Ren, G. Chen, *Energy Environ. Sci.* **2009**, *2*, 466.
[7] D. Narducci, *Appl. Phys. Lett.* **2011**, *99*, 102104.
[8] C. J. Vineis, A. Shakouri, A. Majumdar, M. G. Kanatzidis, *Adv. Mater.* **2010**, *22*, 3970.
[9] G. Tan, L. D. Zhao, M. G. Kanatzidis, *Chem. Rev.* **2016**, *116*, 12123.
[10] J. Q. Guo, H. Y. Geng, T. Ochi, S. Suzuki, M. Kikuchi, Y. Yamaguchi, S. Ito, *J. Electron. Mater.* **2012**, *41*, 1036.
[11] S. J. Poon, *Metals* **2018**, *8*, 989.
[12] J. Shuai, J. Mao, S. Song, Q. Zhang, G. Chen, Z. Ren, *Mater. Today Phys.* **2017**, *1*, 74.
[13] C. H. Su, *Prog. Cryst. Growth Charact. Mater.* **2019**, *65*, 47.
[14] H. Mamur, M. R. A. Bhuiyan, F. Korkmaz, M. Nil, *Renewable Sustainable Energy Rev.* **2018**, *82*, 4159.
[15] J. Pei, B. Cai, H. L. Zhuang, J. F. Li, *Natl. Sci. Rev.* **2020**, *7*, 1856.
[16] C. Wood, *Rep. Prog. Phys.* **1988**, *51*, 459.
[17] M. Bittner, N. Kanas, R. Hinterding, F. Steinbach, J. Räthel, M. Schrade, K. Wiik, M. A. Einarsrud, A. Feldhoff, *J. Power Sources* **2019**, *410–411*, 143.
[18] N. Kanas, S. P. Singh, M. Rotan, M. Saleemi, M. Bittner, A. Feldhoff, T. Norby, K. Wiik, T. Grande, M. A. Einarsrud, *J. Eur. Ceram. Soc.* **2018**, *38*, 1592.
[19] A. Sotelo, S. Rasekh, M. A. Torres, P. Bosque, M. A. Madre, J. C. Diez, *J. Solid State Chem.* **2015**, *221*, 247.
[20] K. A. Sekak, A. Lowe, *J. Am. Ceram. Soc.* **2011**, *94*, 611.
[21] T. Yin, D. Liu, Y. Ou, F. Ma, S. Xie, J. F. Li, J. Li, *J. Phys. Chem. C* **2010**, *114*, 10061.
[22] Z. Qiu, J. Pei, G. Chen, C. Lv, Y. Zhang, Y. Yu, Q. Zhang, *Mater. Lett.* **2015**, *158*, 182.
[23] K. Kruppa, I. I. Maor, F. Steinbach, V. Beilin, M. Mann-Lahav, M. Wolf, G. S. Grader, A. Feldhoff, *J. Am. Ceram. Soc.* **2023**, *106*, 1170.
[24] H. F. Wen, C. Yang, D. G. Yu, X. Y. Li, D. F. Zhang, *Chem. Eng. J.* **2016**, *290*, 263.
[25] H. Fan, T. Zhang, X. Xu, N. Lv, *Sens. Actuators, B* **2011**, *153*, 83.
[26] S. Koombhongse, W. Liu, D. H. Reneker, *J. Polym. Sci., Part B: Polym. Phys.* **2001**, *39*, 2598.
[27] M. Mann-Lahav, M. Halabi, G. E. Shter, V. Beilin, M. Balaish, Y. Ein-Eli, D. R. Dekel, G. S. Grader, *Adv. Funct. Mater.* **2020**, *30*, 1901733.
[28] Z. He, Q. Liu, H. Hou, F. Gao, B. Tang, W. Yang, *ACS Appl. Mater. Interfaces* **2015**, *7*, 10878.
[29] C. Wang, S. Y. Tsou, H. S. Lin, *Colloid Polym. Sci.* **2012**, *290*, 1799.
[30] R. Stepanyan, A. V. Subbotin, L. Cuperus, P. Boonen, M. Dorschu, F. Oosterlinck, M. J. H. Bulters, *Polymer* **2016**, *97*, 428.
[31] A. Koski, K. Yim, S. Shivkumar, *Mater. Lett.* **2004**, *58*, 493.
[32] Y. Y. Zhao, Q. B. Yang, X. F. Lu, C. Wang, Y. Wei, *J. Polym. Sci., Part B: Polym. Phys.* **2005**, *43*, 2190.
[33] Z. Li, Y. Fan, J. Zhan, *Eur. J. Inorg. Chem.* **2010**, *2010*, 3348.
[34] A. Neamnark, R. Rujiravanit, P. Supaphol, *Carbohydr. Polym.* **2006**, *66*, 298.
[35] P. Jing, J. Du, J. Wang, J. Wei, L. Pan, J. Li, Q. Liu, *Sci. Rep.* **2015**, *5*, https://doi.org/10.1038/srep15089.
[36] M. T. Zafarani-Moattar, Z. Khoshsima, *J. Chem. Thermodyn.* **2008**, *40*, 1569.
[37] N. Bhardwaj, S. C. Kundu, *Biotechnol. Adv.* **2010**, *28*, 325.
[38] O. Elishav, L. Poliak, I. Naamat, V. Beilin, G. E. Shter, G. S. Grader, *Materials* **2019**, *12*, 252.
[39] O. Elishav, V. Beilin, G. E. Shter, O. Dinner, V. Halperin, G. S. Grader, *J. Am. Ceram. Soc.* **2017**, *100*, 3370.
[40] I. I. Maor, S. Heyte, O. Elishav, M. Mann-Lahav, J. Thuriot-Roukos, S. Paul, G. S. Grader, *Nanomaterials* **2023**, *13*, 635.
[41] D. H. Reneker, A. L. Yarin, *Polymer* **2008**, *49*, 2387.
[42] A. Gevorkyan, G. E. Shter, Y. Shmueli, A. Buk, R. Meir, G. S. Grader, *J. Mater. Res.* **2014**, *29*, 1721.
[43] B. Ghorani, N. Tucker, *Food Hydrocolloids* **2015**, *51*, 227.
[44] O. Elishav, V. Beilin, O. Rozent, G. E. Shter, G. S. Grader, *J. Polym. Sci., Part B: Polym. Phys.* **2018**, *56*, 248.
[45] O. Rozent, V. V. Beilin, G. E. Shter, G. S. Grader, *J. Am. Ceram. Soc.* **2016**, *99*, 1550.
[46] S. Fitzpatrick, J. F. McCabe, C. R. Petts, S. W. Booth, *Int. J. Pharm.* **2002**, *246*, 143.
[47] J. Teng, S. Bates, D. A. Engers, K. Leach, P. Schields, Y. Yang, *J. Pharm. Sci.* **2010**, *99*, 3815.
[48] Y. Miyazaki, M. Onoda, T. Oku, M. Kikuchi, Y. Ishii, Y. Ono, Y. Morii, T. Kajitani, *J. Phys. Soc. Jpn.* **2002**, *71*, 491.
[49] K. Koumoto, R. Funahashi, E. Guilmeau, Y. Miyazaki, A. Weidenkaff, Y. Wang, C. Wan, *J. Am. Ceram. Soc.* **2013**, *96*, https://doi.org/10.1111/jace.12076.
[50] H. Itahara, C. Xia, Y. Seno, J. Sugiyama, T. Tani, K. Koumoto, in Proc. 22nd Int. Conf. Thermoelectr. ICT, La Grande Motte, France, **2003**, p. 188.
[51] D. Kenfaui, B. Lenoir, D. Chateigner, B. Ouladdiaf, M. Gomina, J. G. Noudem, *J. Eur. Ceram. Soc.* **2012**, *32*, 2405.
[52] L. Li, S. Peng, Y. Cheah, Y. Ko, P. Teh, G. Wee, C. Wong, M. Srinivasan, *Chem. - Eur. J.* **2013**, *19*, 14823.
[53] M. Bittner, L. Helmich, F. Nietschke, B. Geppert, O. Oeckler, A. Feldhoff, *J. Eur. Ceram. Soc.* **2017**, *37*, 3909.
[54] Y. Liu, Y. Lin, Z. Shi, C. W. Nan, Z. Shen, *J. Am. Ceram. Soc.* **2005**, *88*, 1337.
[55] S. Bresch, B. Mieller, D. Schönauer-Kamin, R. Moos, T. Reimann, F. Giovannelli, T. Rabe, *J. Am. Ceram. Soc.* **2021**, *104*, 917.
[56] J. Y. Cho, O. J. Kwon, Y. K. Chung, J. S. Kim, W. S. Kim, K. J. Song, C. Park, *J. Electron. Mater.* **2015**, *44*, 3621.
[57] R. Hinterding, D. Rieks, P. A. Kißling, L. Steinbach, N. C. Bigall, A. Feldhoff, *J. Electron. Mater.* **2022**, *51*, 532.
[58] C. M. Fancher, *Materials* **2021**, *14*, 5633.
[59] D. Kenfaui, D. Chateigner, M. Gomina, J. G. Noudem, *Int. J. Appl. Ceram. Technol.* **2011**, *8*, 214.
[60] H. Itahara, J. Sugiyama, T. Tani, *Jpn. J. Appl. Phys., Part 1* **2004**, *43*, 5134.
[61] W. H. Yoon, J. Ryu, J. J. Choi, B. D. Hahn, J. H. Choi, B. K. Lee, J. H. Cho, D. S. Park, *J. Am. Ceram. Soc.* **2010**, *93*, 2125.
[62] M. Bittner, N. Kanas, R. Hinterding, F. Steinbach, D. Groeneveld, P. Wemhoff, K. Wiik, M. A. Einarsrud, A. Feldhoff, *J. Eur. Ceram. Soc.* **2019**, *39*, 1237.
[63] Z. Shi, J. Xu, J. Zhu, Y. Zhang, T. Gao, M. Qin, H. Sun, G. Dong, F. Gao, *Ceram. Int.* **2019**, *45*, 1977.
[64] T. Schulz, T. Reimann, A. Bochmann, A. Vogel, B. Capraro, B. Mieller, S. Teichert, J. Töpfer, *J. Eur. Ceram. Soc.* **2018**, *38*, 1600.
[65] J. Maier, *Physical Chemistry of Ionic Materials: Ions and Electrons in Solids*, Wiley, Chichester **2004**.
[66] J. Yu, R. Freer, *JPhys Energy* **2022**, *4*, https://doi.org/10.1088/2515-7655/ac5172.
[67] M. Wolf, K. Menekse, A. Mundstock, R. Hinterding, F. Nietschke, O. Oeckler, A. Feldhoff, *J. Electron. Mater.* **2019**, *48*, 7551.

© 2023 The Authors. Advanced Functional Materials published by Wiley-VCH GmbH

16163028, 0, Downloaded from https://onlinelibrary.wiley.com/doi/10.1002/adfm.202304464 by Cochrane Germany, Wiley Online Library on [22/11/2023]. See the Terms and Conditions (https://onlinelibrary.wiley.com/terms-and-conditions) on Wiley Online Library for rules of use; OA articles are governed by the applicable Creative Commons License